



Sound velocity and elastic properties of Fe–Ni–S–Si liquid: the effects of pressure and multiple light elements

Iori Yamada¹ · Hidenori Terasaki² · Satoru Urakawa² · Tadashi Kondo¹ · Akihiko Machida³ · Yoshinori Tange⁴ · Yuji Higo⁴

Received: 19 March 2023 / Accepted: 28 May 2023
© The Author(s) 2023

Abstract

Fe–Ni–S–Si alloy is considered to be one of the plausible candidates of Mercury core material. Elastic properties of Fe–Ni–S–Si liquid are important to reveal the density profile of the Mercury core. In this study, we measured the P-wave velocity (V_p) of Fe–Ni–S–Si ($\text{Fe}_{73}\text{Ni}_{10}\text{S}_{10}\text{Si}_7$, $\text{Fe}_{72}\text{Ni}_{10}\text{S}_5\text{Si}_{13}$, and $\text{Fe}_{67}\text{Ni}_{10}\text{S}_{10}\text{Si}_{13}$) liquids up to 17 GPa and 2000 K to study the effects of pressure, temperature, and multiple light elements (S and Si) on the V_p and elastic properties.

The V_p of Fe–Ni–S–Si liquids are less sensitive to temperature. The effect of pressure on the V_p are close to that of liquid Fe and smaller than those of Fe–Ni–S and Fe–Ni–Si liquids. Obtained elastic properties are $K_{S0} = 99.1(9.4)$ GPa, $K_S' = 3.8(0.1)$ and $\rho_0 = 6.48$ g/cm³ for S-rich $\text{Fe}_{73}\text{Ni}_{10}\text{S}_{10}\text{Si}_7$ liquid and $K_{S0} = 112.1(1.5)$ GPa, $K_S' = 4.0(0.1)$ and $\rho_0 = 6.64$ g/cm³ for Si-rich $\text{Fe}_{72}\text{Ni}_{10}\text{S}_5\text{Si}_{13}$ liquid. The V_p of Fe–Ni–S–Si liquids locate in between those of Fe–Ni–S and Fe–Ni–Si liquids. This suggests that the effect of multiple light element (S and Si) on the V_p is suppressed and cancel out the effects of single light elements (S and Si) on the V_p . The effect of composition on the EOS in the Fe–Ni–S–Si system is indispensable to estimate the core composition combined with the geodesy data of upcoming Mercury mission.

Keywords Fe alloy · Sound velocity · Liquid · Core · Mercury · Light element

Introduction

The cores of terrestrial planets such as Mercury, Earth, and Mars are considered to consist of Fe–Ni alloy with some amount of light elements, such as S, Si, C, O, and H (e.g., Hauck et al. 2013; Hirose et al. 2013; Yoshizaki and McDonough 2020). Mercury is thought to have large core fraction (58–68 mass%), which is much larger than those of other terrestrial planets, from the bulk density and moment of inertia of Mercury (e.g., Hauck et al. 2013) and have a molten core based on Earth-based radar measurements (Margot

et al. 2007). X-ray spectrometer in MESSENGER (Mercury Surface ENvironment GEochemistry and Ranging) spacecraft found that Mercury surface has high Mg/Si ratio and contains 1–4 wt% of sulfur (Nittler et al. 2011). High Mg/Si ratio reflects Mercury formed from highly reduced precursor materials, suggesting that Mercury core contains substantial Si as well as S (Smith et al. 2012). Furthermore, if the S abundance of Mercury surface (1–4 wt%) is representative of bulk silicate composition, metal-silicate partition experiments suggest that the core-forming melts in early stage magma ocean contain both S and Si (Chabot et al. 2014). Therefore, Mercury's core most likely contains both S and Si.

In the Fe–S–Si system, there are immiscible region, i.e., miscibility gap, in the liquid phase at ambient pressure. The miscibility gap shrinks with increasing pressure (Morard and Katsura 2010). The estimated possible range of Mercury core composition in the Fe–S–Si system corresponds to be the miscible region at the core conditions (6–40 GPa) as shown in Fig. 1 (Chabot et al. 2014). Therefore, the equation of state (EOS) of the Fe–Ni–S–Si miscible liquid is required for understanding the size and

✉ Hidenori Terasaki
tera@okayama-u.ac.jp

¹ Department of Earth and Space Science, Osaka University, Osaka, Japan

² Department of Earth Sciences, Okayama University, Okayama, Japan

³ Synchrotron Radiation Research Center, National Institutes for Quantum Science and Technology (QST), Hyogo, Japan

⁴ Japan Synchrotron Radiation Research Institute, Hyogo, Japan

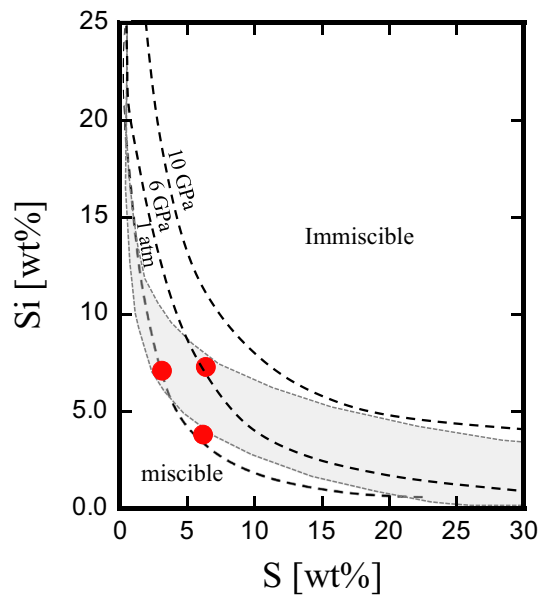


Fig. 1 Used sample compositions and miscible/immiscible boundary in the Fe–S–Si system. Used sample compositions are shown by red circles. $\text{Fe}_{73}\text{Ni}_{10}\text{S}_{10}\text{Si}_7$, $\text{Fe}_{72}\text{Ni}_{10}\text{S}_5\text{Si}_{13}$ and $\text{Fe}_{72}\text{Ni}_{10}\text{S}_{10}\text{Si}_{13}$ in atomic ratio correspond to Fe–11.3wt%Ni–6.2wt%S–3.8wt%Si, Fe–11.4wt%Ni–3.1wt%S–7.1wt%Si, Fe–11.7wt%Ni–6.4wt%S–7.3wt%Si, respectively. Dashed curves show the miscible/immiscible boundary in the Fe–S–Si system at 1 atm, 6, and 10 GPa (Morard and Katsura 2010). Shaded area denotes possible range of Mercury core composition with producing 1–4 wt% S in the silicate, as measured on the Mercury surface (Chabot et al. 2014)

composition of Mercury core combined with observed geodesy data.

The effects of pressure and temperature on the density and sound velocity of Fe–Ni–S–Si liquid are needed to determine its EOS. The effect of a single alloying element on the P-wave velocity (V_p) of Fe and Fe–Ni liquid has been studied at 1 atm and high pressures in various systems (Fe–(Ni)–S, Fe–(Ni)–C, Fe–(Ni)–Si) (Nasch et al. 1997; Nishida et al. 2013, 2016, 2020; Jing et al. 2014; Kuwabara et al. 2016; Shimoyama et al. 2016; Nakajima et al. 2015; Kawaguchi et al. 2017; Terasaki et al. 2019). Ni reduces the V_p of pure Fe liquid (Kuwabara et al. 2016). Si increases the V_p of Fe–Ni liquid (Terasaki et al. 2019). On the contrary, the V_p of pure Fe and Fe–Ni liquid decreases with increasing S content (Nishida et al. 2013, 2016, 2020; Jing et al. 2014; Kawaguchi et al. 2017; Terasaki et al. 2019). However, the effect of simultaneous dissolution of S and Si in liquid Fe and Fe–Ni on the V_p or elastic property has not been investigated. In this study, we measured the V_p of liquid Fe–Ni–S–Si up to 17 GPa to study the effect of both pressure and multiple light elements (S and Si) on the V_p and elastic properties and discuss the EOS of Fe–Ni–S–Si liquid.

Experimental

We used Fe–Ni–S–Si sample with three different compositions (S-rich: $\text{Fe}_{73}\text{Ni}_{10}\text{S}_{10}\text{Si}_7$, Si-rich: $\text{Fe}_{72}\text{Ni}_{10}\text{S}_5\text{Si}_{13}$, and S&Si-rich: $\text{Fe}_{67}\text{Ni}_{10}\text{S}_{10}\text{Si}_{13}$ in at%). The samples were powder mixtures of Fe (99.9% in purity, Wako Pure Chemical Co., Ltd), Ni (99.9%, Rare Metallic Co., Ltd), FeS (99.9%, Rare Metallic Co., Ltd), and FeSi (99.9%, Rare Metallic Co., Ltd). The used compositions are in the range of possible Mercury core composition suggested by Chabot et al. (2014) as shown in Fig. 1. S-rich and Si-rich compositions of this study locate near the liquid miscible–immiscible boundary at ambient pressure and S&Si-rich composition locates at the immiscible boundary at 6 GPa. Since the liquid immiscible region shrinks at higher pressure (Morard and Katsura, 2010), the sample used in this study melts into a miscible liquid at the pressure conditions of this study (S-rich: 3–16 GPa, Si-rich: 4–13 GPa, S&Si-rich: 17 GPa).

The P-wave velocity (V_p) measurements at high pressure were performed using 180 ton DIA-type cubic multianvil press (SMAP-180) at BL22XU beamline (Shobu et al. 2007) or using 1500ton Kawai-type multianvil press (SPEED-Mk. II) at BL04B1 (Higo et al. 2009), SPring-8 synchrotron facility. DIA-type press with an anvil top size of 6 mm was used in the measurement below 5 GPa and Kawai-type press with a truncated edge length of 2nd stage anvil of 5 mm was used in the measurement above 5 GPa. Details of used cell assemblies are described in Terasaki et al. (2019). The sample was sandwiched by the single-crystal sapphire buffer rod for V_p measurement. High temperature was generated using cylindrical graphite heater below 5 GPa and TiC– Al_2O_3 composite heater above 5 GPa. The experimental pressures and temperatures were determined from lattice volumes of two pressure markers (BN and MgO below 5 GPa and NaCl and MgO above 5 GPa) with their equations of state (BN: Wakabayashi and Funamori, 2015, MgO: Tange et al. 2009, NaCl: Matsui 2009). The lattice volumes were determined from X-ray diffraction (XRD) measurement. The uncertainties of experimental pressures and temperatures are derived from errors of lattice volumes of the pressure markers. At BL22XU, a monochromatic X-ray of 35 keV was used and XRD was collected using a flat panel detector (C7942CK-12, Hamamatsu Co Ltd.) with an angle-dispersive method. At BL04B1, white X-ray was used and XRD was collected using a Ge solid-state detector with an energy-dispersive method at 2θ angle of 6° . In the present study, all the V_p measurements were performed in the molten state of the sample. The sample state was checked from disappearance of sample diffraction peaks and appearance of diffuse scattering signal. The experimental conditions of this study are listed in Table 1.

Table 1 Experimental conditions and V_p data obtained in this study

Composition	Run No	P (GPa)	T (K)	V_p (km/s)	ρ (g/cm ³)
Fe ₇₃ Ni ₁₀ S ₁₀ Si ₇ (S-rich)	B283	3.2 ±0.1	1620 ±30	4.09 ±0.19	6.68 ±0.03
	B291	4.3 ±0.1	1940 ±20	4.13 ±0.09	
	M2230	13.8 ±0.1	1940 ±20	4.44 ±0.11	
	M2320	±0.1 14.8	1940 ±30	4.67 ±0.19	
	M2669	16.1 ±0.2	2010 ±50	4.63 ±0.12	
	M2669	16.3 ±0.3	1830 ±90	4.63 ±0.15	
	B292	4.4 ±0.1	1740 ±20	4.34 ±0.07	
Fe ₇₂ Ni ₁₀ S ₅ Si ₁₃ (Si-rich)	B292	4.9 ±0.1	1810 ±20	4.35 ±0.09	6.91 ±0.03
	M2668	13.0 ±0.3	1910 ±90	4.69 ±0.38	
	M2668	13.3 ±0.2	1720 ±60	4.74 ±0.40	
	M2874	17.1 ±0.2	1770 ±70	4.89 ±0.44	

V_p was measured using ultrasonic pulse-echo overlapping method (e.g., Higo et al. 2009). The V_p is determined from $V_p = 2L/\Delta t$, where L is a sample length and Δt is two-way travel time of the ultrasonic wave in the sample. LiNbO₃ transducer was attached on the back side of the tungsten carbide anvil to generate and receive ultrasonic waves. The electric signals of sine waves with frequencies of 37–55 MHz were formed using a waveform generator (AFG3251C, Tektronix Inc.) and were input to the transducer. The ultrasonic echo signals from the sample interfaces were detected by the high resolution digital oscilloscope (DPO5054 and MDO4104C, Tektronix Inc.) with a sampling rate of 5×10^9 sample/s. Figure 2(a)(b) is typical example of measured echo signals from the sample interfaces. The difference in arrival times of echo signals from the sample front and back interfaces corresponds two-way travel time in the sample (Δt). Details of waveform analysis are described elsewhere (Kono et al. 2012). The sample length was measured from X-ray radiography image (inset of Fig. 2(a)(b)). X-ray radiography image was observed using CMOS camera (orca-flashV4, Hamamatsu Co Ltd.) with a YAG scintillator. The pixel sizes of the image were 1.5–3.0 μm .

In order to obtain constraint for equation of state of the liquid Fe–Ni–S–Si samples, we also measured sample densities at a certain pressure. The density was measured using X-ray absorption method at BL22XU beamline (e.g., Shimoyama et al. 2016). In this method, intensities of incident X-ray (I_0) and transmitted X-ray (I) were measured using

ion chambers and X-ray absorption profile along the radial direction of cylindrical sample were obtained as shown in Fig. 2(c). Then, following Beer–Lambert law is used to deduce sample density;

$$I = I_0 \exp\left[(-\mu\rho t)_{\text{Sample}} + (-\mu\rho t)_{\text{Capsule}} + (-\mu\rho t)_{\text{Environment}}\right], \quad (1)$$

where μ , ρ and t denote mass absorption coefficient, density, and thickness in X-ray direction, respectively. The ρ of sample was obtained by fitting the measured X-ray absorption profile of both sample and sample capsule using Eq. (1). The third "Environment" term represents the contribution of the materials surrounding the sample capsule. The second and third terms of Eq. (1) can be obtained from X-ray intensity at the sample/capsule boundary. The μ of the sample was obtained from X-ray absorption profiles of the cold pressed solid samples and their densities determined from XRD. The μ of the capsule was referred from NIST Standard Reference database (<https://doi.org/10.18434/T4HS32>). Details of X-ray absorption method are described elsewhere (Shimoyama et al. 2016; Terasaki and Nishida 2018).

Recovered samples were mounted in epoxy resin and polished for textural observation and chemical composition analysis. Textural observation and chemical analysis were carried out using a scanning electron microscope (SEM, JSM-6010LA, JEOL Ltd.) equipped with energy-dispersive spectroscopy (EDS) detector (UltraDry, Thermo Fischer Scientific K.K.) installed at Osaka university.

Fig. 2 Typical examples of measured echo signals and X-ray absorption profile of the Fe–Ni–S–Si liquid samples. **a** Measured echo signal of $\text{Fe}_{72}\text{Ni}_{10}\text{S}_5\text{Si}_{13}$ sample at 4.4 GPa and 1740 K (B292) and **b** that of $\text{Fe}_{73}\text{Ni}_{10}\text{S}_{10}\text{Si}_7$ sample at 16.1 GPa and 2010 K (M2669). Inset indicates the radiography image of the sample. Δt and L represent two-way travel time and sample length, respectively. **c** X-ray absorption profile of $\text{Fe}_{72}\text{Ni}_{10}\text{S}_5\text{Si}_{13}$ sample at 4.4 GPa and 1740 K (B292). Black dot and red curve denote measured I/I_0 data and fitted curve using Beer–Lambert law, respectively

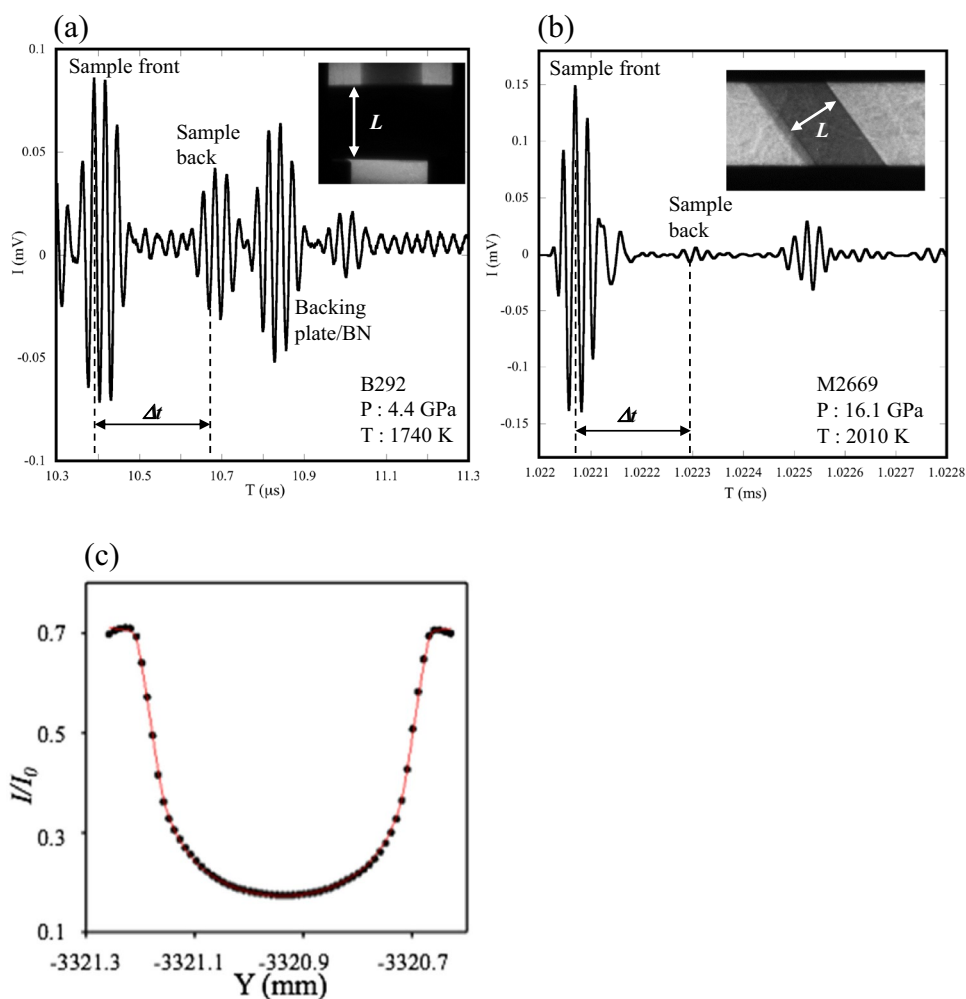
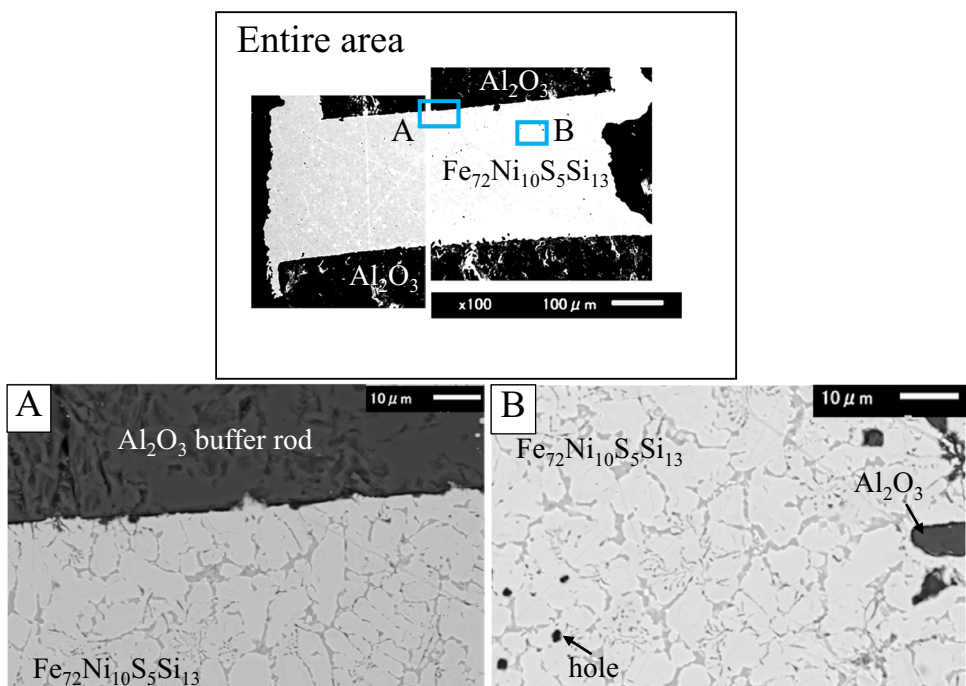


Fig. 3 Backscattered electron image of $\text{Fe}_{72}\text{Ni}_{10}\text{S}_5\text{Si}_{13}$ sample (M2668) recovered from 13 GPa and 1910 K. Duration time in the liquid state was approximately 30 min. Entire part of the sample is shown in top panel and magnified images are shown in bottom. The $\text{Fe}_{72}\text{Ni}_{10}\text{S}_5\text{Si}_{13}$ sample shows homogeneous quenched texture. Dark gray area indicate Al_2O_3 buffer rod. Although some small bits of Al_2O_3 were observed especially near the boundary between the sample and buffer rod, there is no reaction rim at the boundary between the sample and buffer rod



Results and discussion

The effects of temperature and pressure

The experimental conditions of this study and measured P-wave velocity (V_p) and density of liquid Fe–Ni–S–Si are summarized in Table 1. The error of the V_p is derived from error of the travel time and that of sample length. The error of travel time is 0.3–0.7%, caused by overlapping echo signals between sample front and back. The error of sample length is 1.3–7.9%, caused by sharpness of a boundary between sample and buffer rod and also by variation in sample length. Figure 3 shows a backscattered electron image of the recovered Fe–Ni–S–Si sample from 13 GPa and 1910 K. The sample shows homogeneous quench texture, indicating that the sample was a miscible liquid at the present experimental conditions. A boundary between the sample and single-crystal Al_2O_3 buffer rod was clear as shown in Fig. 3. Although small bits of Al_2O_3 were observed near the boundary between the sample and buffer rod, Al_2O_3 component was not detected in Fe–Ni–S–Si sample from EDS measurement suggesting that there was no chemical reaction between the sample and buffer rod.

The effect of temperature on the V_p of two sample compositions (S-rich: $Fe_{73}Ni_{10}S_{10}Si_7$, Si-rich: $Fe_{72}Ni_{10}S_5Si_{13}$) is plotted in Fig. 4. The temperature dependence on V_p is quite small in both S-rich and Si-rich liquids. It has been reported that the V_p of Fe–10 wt%Ni is insensitive to temperature (Kuwabara et al. 2016) and that of $Fe_{57}S_{43}$ and $Fe_{84}S_{16}$ nearly independent of temperature (Nishida et al. 2013; Jing et al. 2014). Although liquid Fe–Ni–Si (Si = 6–20 wt%) and Fe has negative gentle temperature dependence (Fe–Ni–Si: $\frac{dV_p}{dT}$

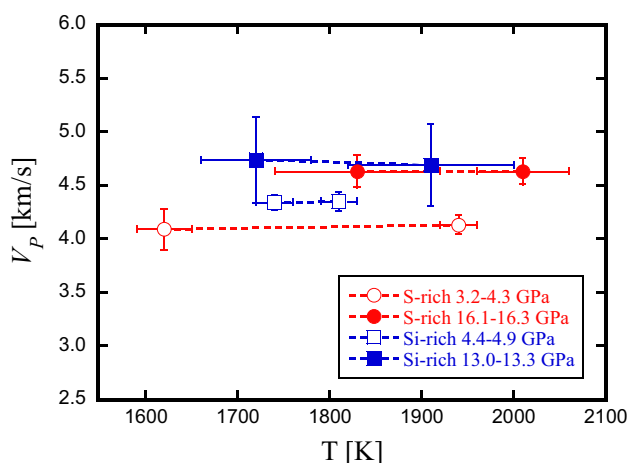


Fig. 4 Temperature dependence of V_p of Fe–Ni–S–Si liquids. Red and blue symbols represent $Fe_{73}Ni_{10}S_{10}Si_7$ (S-rich) and $Fe_{72}Ni_{10}S_5Si_{13}$ (Si-rich) liquids, respectively. Pressure conditions are written in legend

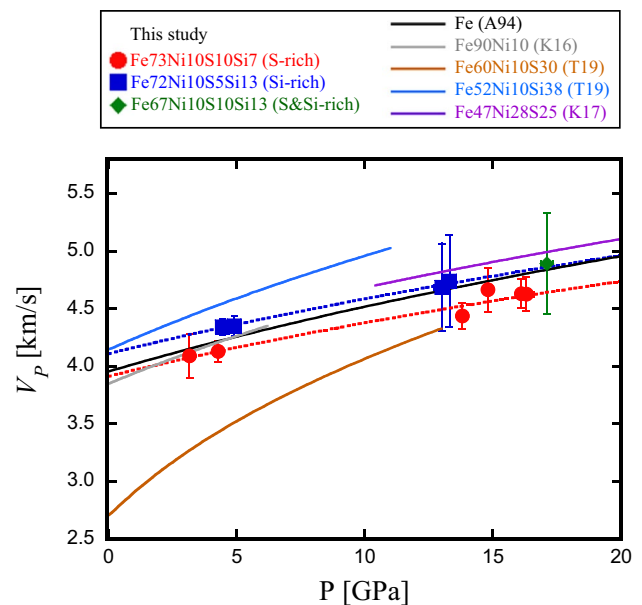


Fig. 5 Pressure dependence of V_p Fe–Ni–S–Si liquids. Red, blue, green symbols represent $Fe_{73}Ni_{10}S_{10}Si_7$ (S-rich), $Fe_{72}Ni_{10}S_5Si_{13}$ (Si-rich), and $Fe_{67}Ni_{10}S_{10}Si_{13}$ (S&Si-rich) liquids, respectively. Dotted curves indicate fitting to the present V_p data using third-order Birch–Murnaghan EOS. Solid curves show V_p of various Fe-alloy liquids calculated based on reported elastic parameters with third-order Birch–Murnaghan EOS. Black: Fe (Anderson and Ahrens 1994), grey: $Fe_{90}Ni_{10}$ (Kuwabara et al. 2016), brown: $Fe_{60}Ni_{10}S_{30}$ (Terasaki et al. 2019), purple: $Fe_{47}Ni_{28}S_{25}$ (Kawaguchi et al. 2017), and light blue: $Fe_{52}Ni_{10}Si_{38}$ (Terasaki et al. 2019)

$= -0.333 \sim -0.504$ m/s/K, Fe: $\frac{dV_b}{dT} = -0.54$ m/s/K, where V_b is bulk sound velocity) (Williams et al. 2015; Anderson and Ahrens 1994), liquid Fe–Ni–S–Si in this study shows similar temperature dependences of liquid Fe–Ni and Fe–S.

The V_p of liquid Fe–Ni–S–Si are plotted as a function of pressure in Fig. 5. The V_p of both S-rich and Si-rich Fe–Ni–S–Si liquids increase with pressure. The pressure dependence, dV_p/dP , of Fe–Ni–S–Si liquids (both S-rich and Si-rich) are smaller than those of Fe–Ni–S and Fe–Ni–Si liquids and close to that of Fe (Anderson and Ahrens 1994) and $Fe_{47}Ni_{28}S_{25}$ (Kawaguchi et al. 2017) liquids as shown in Fig. 5. The V_p of Si-rich liquid is larger than that of S-rich liquid in present pressure range. It has been reported that addition of S decreases the V_p , while addition of Si increases it in the present pressure range at least below 10–14 GPa (e.g., Jing et al. 2014; Terasaki et al. 2019). Compared to previous studies, V_p of Fe–Ni–S–Si liquids of this study locate in between the V_p of $Fe_{60}Ni_{10}S_{30}$ and $Fe_{52}Ni_{10}Si_{38}$ liquids (Terasaki et al. 2019) as shown in a Fig. 5. The V_p of S-rich liquid of this study is approximately 2% smaller and that of Si-rich liquid is ~3% larger than the V_p of liquid Fe–10wt%Ni at 4.3–4.4 GPa (Kuwabara et al. 2016). Thus, the effect of S or Si on the V_p of liquid Fe–Ni–S–Si

is suppressed compared to those of liquid Fe–Ni–S and Fe–Ni–Si. This suggests that the effect of S and Si on the V_p could be cancelled out each other. Detailed effect of light elements will be discussed in later section.

Elastic properties

To consider the pressure dependence of the V_p and estimate elastic properties of the liquids, we fitted the V_p data using second-order and third-order Birch–Murnaghan equations of state (EOS) as shown below. Since the effect of temperature on the V_p of the present liquids are negligibly small, the V_p data at all the temperature conditions are fitted together. The relationship between V_p and density (ρ) in liquid is expressed as,

$$V_p = \sqrt{\frac{K_S}{\rho}}, \tag{2}$$

where K_S is adiabatic bulk modulus.

The third-order Birch–Murnaghan EOS (3BM) is described as

$$P = \frac{3}{2}K_{S0} \left[\left(\frac{\rho}{\rho_0} \right)^{\frac{7}{3}} - \left(\frac{\rho}{\rho_0} \right)^{\frac{5}{3}} \right] \left[1 + \frac{3}{4}(K_{S0}' - 4) \left\{ \left(\frac{\rho}{\rho_0} \right)^{\frac{2}{3}} - 1 \right\} \right] \tag{3}$$

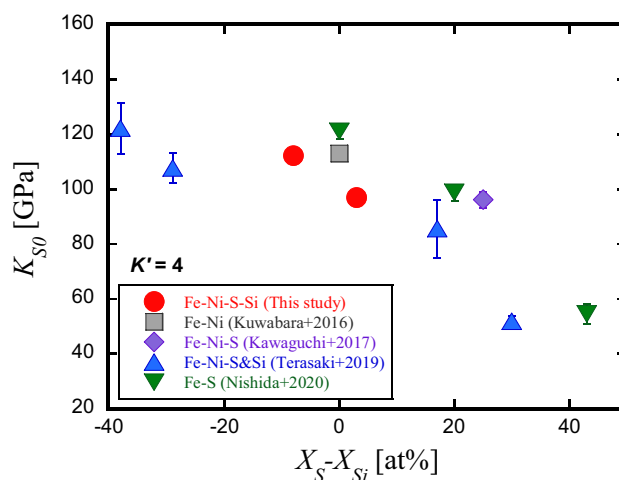


Fig. 6 K_{S0} plotted as a function of difference between S content (X_S) and Si content (X_{Si}) in at%. The K_{S0} of Fe–Ni–S–Si liquid in this study are listed in Table 2. The K_{S0} of previous studies were obtained by fitting the data with $K_S' = 4$. The compositions of previous studies are Fe₉₀Ni₁₀ by Kuwabara et al. (2016), Fe₄₇Ni₂₈S₂₅ by Kawaguchi et al. (2017), Fe₇₃Ni₁₀S₁₇, Fe₆₀Ni₁₀S₃₀, Fe₆₁Ni₁₀Si₂₉, and FeNi₁₀Si₃₈ by Terasaki et al. (2019), Fe, Fe₈₀S₂₀, and Fe₅₇S₄₃ by Nishida et al. (2020)

Table 2 Adiabatic elastic properties of this study and previous studies

Composition	K_{S0} (GPa)	K_S'	ρ_0 (g/cm ³)	T_0 (K)	EOS ^c	References
Fe ₇₃ Ni ₁₀ S ₁₀ Si ₇	99.1 ± 9.4	3.8 ± 0.1	6.48 ^a	1620	3BM	This study
	96.9 ± 1.8	4.0 (fix)	6.48 ^a	1620	2BM	This study
Fe ₇₂ Ni ₁₀ S ₅ Si ₁₃	± 1.5	4.0	6.64 ^b	1810	3BM	This study
	112.1 ± 0.1	± 0.1 (fix)	6.64 ^b	1810	2BM	This study
	112.1 ± 0.1	4.0 (fix)	6.64 ^b	1810	2BM	This study
Fe	109.7 ± 0.7	4.7	7.02	1811	3BM	Anderson & Ahrens (1994)
Fe ₉₀ Ni ₁₀	103.0 ± 2.0	5.7 ± 0.8	6.97	1900	M	Kuwabara et al. (2016)
Fe ₆₀ Ni ₁₀ S ₃₀	38.1 ± 1.8	7.4 ± 0.2	5.21	1650	3BM	Terasaki et al. (2019)
Fe ₄₇ Ni ₂₈ S ₂₅	96.1 ± 2.7	4.0 ± 0.1	5.62	2000	M	Kawaguchi et al. (2017)
Fe ₅₂ Ni ₁₀ Si ₃₈	102.1 ± 1.1	7.8 ± 0.1	5.95	1550	3BM	Terasaki et al. (2019)

^aReference density of 6.68 g/cm³ at 3.2 GPa was used

^bReference density of 6.91 g/cm³ at 4.9 GPa was used

^cUsed EOS to fit the V_p data; 3BM: 3rd order Birch-Murnaghan EOS, 2BM: 2nd order Birch-Murnaghan EOS, M: Murnaghan EOS

$$K_S = K_{S0} \left(\frac{\rho}{\rho_0}\right)^{\frac{5}{3}} \left[1 + \frac{1}{2} (3K'_{S0} - 5) \left\{ \left(\frac{\rho}{\rho_0}\right)^{\frac{2}{3}} - 1 \right\} + \frac{27}{8} (K'_{S0} - 4) \left\{ \left(\frac{\rho}{\rho_0}\right)^{\frac{2}{3}} - 1 \right\}^2 \right] \tag{4}$$

where K_{S0} and K'_S are adiabatic bulk modulus at ambient pressure and its pressure derivative, respectively. Then, from Eqs. (2) and (4), V_p can be expressed as a function of pressure. The second-order Birch–Murnaghan EOS (2BM) can be obtained if we assume $K'_{S0} = 4$. In this study, we directly measured density at low pressures (3–5 GPa, Table 1) and this measured density is used as a reference density (ρ_{ref}) at reference pressure instead of ρ_0 at ambient pressure in Eqs. (3),(4) (e.g., Sata et al. 2002). Then, we fitted the V_p data using 2BM or 3BM EOS with ρ_{ref} to obtain K_{S0} and K'_S .

Obtained elastic properties and those of previous studies are listed in Table 2. In terms of K_{S0} , it is reported that K_{S0} of Fe–Ni reduces (approximately 63%) by addition of 30 at% S, while it stays constant (~ 1%) even by addition 38 at% Si (Terasaki et al. 2019). To understand the effect of S and Si on the K_{S0} correctly, we need to compare the K_{S0} with using same K'_S since there is tradeoff relation between K_{S0} and K'_S . Figure 6 shows the K_{S0} of this study plotted as a function of difference between S and Si contents ($X_S - X_{Si}$), i.e., relative concentration of light elements. The K_{S0} of previous studies were re-estimated by fitting the data with $K'_S = 4$ and also plotted in Fig. 6. The K_{S0} tends to decrease significantly with increasing S content and increases with increasing Si content. It is found that Fe–Ni–S–Si liquid of this study align in the

same trend of the Fe–Ni liquids with single light element (Fe–Ni–S and Fe–Ni–Si). This suggests a variation of K_{S0} of Fe–Ni–S–Si liquid simply follows concentrations of S and Si.

The effect of light elements

To evaluate the effect of two light elements (S and Si) alloying on the density and V_p quantitatively, we compare the results of this study with reported mixing model of Fe–FeS binary liquid alloy system. In the ideal mixing model, volume (V) of liquid alloy is described as,

$$V = (1 - x)V_1 + xV_2, \tag{5}$$

where V_i and x , respectively, represent a partial molar volume of end-member component i (Fe and FeS) and a mole fraction of end-member component 2. Using the mixing model, the density (ρ), thermal expansivity (α), and isothermal bulk modulus (K_T) of liquid alloy can be expressed using those of the end-member component as follows (e.g., Rivoldini et al. 2011),

$$\rho = \frac{(1 - x)M_1 + xM_2}{V}, \alpha = \frac{1}{V} ((1 - x)V_1\alpha_1 + xV_2\alpha_2)_P, \tag{6}$$

$$K_T = V \left[\frac{(1 - x)V_1}{K_{T,1}} + \frac{xV_2}{K_{T,2}} \right]^{-1},$$

where M_i is molar mass of end-member component i . Then, the V_p can be calculated from the $K_S (= (1 + \alpha\gamma T)K_T$, where γ denotes Grüneisen parameter) and ρ using Eq. (2). Used parameters of the end-member components in the mixing model are referred from Table 5 in Terasaki et al. (2019).

The V_p as a function of S content of the Fe–FeS liquids at 1 atm and 20 GPa and at 1811 K, calculated based on the mixing model, are shown in Fig. 7. The V_p from the Fe–FeS mixing model at 20 GPa is consistent with that of $Fe_{57}S_{43}$ liquid measured at 20 GPa (Nishida et al. 2020). The V_p of Fe–Ni–S–Si liquids at 1 atm and 20 GPa and at 1811 K, calculated by Eqs. (3) and (4) using the elastic data from this study (Table 2), are also plotted. At 1 atm, the V_p gap between the Fe–Ni–S–Si liquid and Fe–FeS binary liquid are quite large. At 20 GPa, the V_p of Fe–Ni–S–Si liquid becomes closer to the Fe–FeS binary liquid. Since the V_p gap between the Fe–Ni–S–Si and Fe–FeS binary liquids could be an influence of Si dissolution, the results may suggest that the effect of Si on the V_p of Fe–Ni–S liquid becomes smaller at higher pressure.

In the local structure of liquid Fe-alloys, S incorporates as an interstitial atom in Fe lattice, while Si substitutes the Fe site up to at least 5 GPa (Shibazaki and Kono 2018). Below 16 at% of S, S incorporates interstitially, increasing neighboring atomic distances and causing softening of the Fe–S liquid. On the contrary, when Si substitutes Fe atoms,

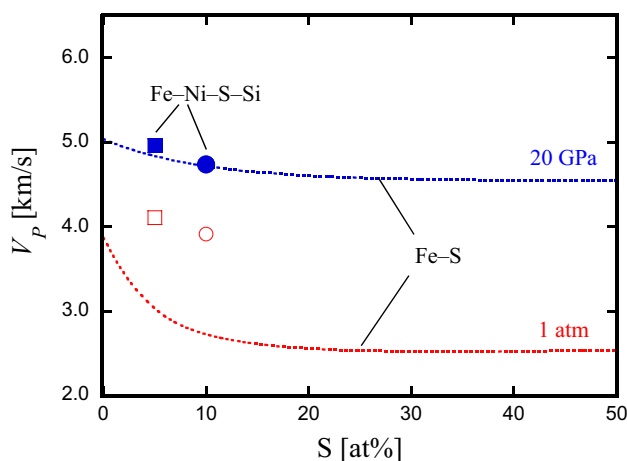


Fig. 7 The effect of S content on the V_p at 1 atm (red) and 20 GPa (blue) at 1811 K. Dashed curves represent Fe–FeS ideal mixing model. Circle and square symbols, respectively, indicate the data of $Fe_{73}Ni_{10}S_{10}Si_7$ and $Fe_{72}Ni_{10}S_5Si_{13}$ calculated from the obtained EOS in this study (see Table 2) (Red open and blue closed symbols denote the data at 1 atm and 20 GPa). Parameters used in the mixing model are given in Table 5 in Terasaki et al. (2019)

the nearest and 2nd neighbor distances are shortened causing stiffening of the Fe–Si liquid. Existence of liquid immiscibility in the Fe–S–Si system could be attributed to the strong covalency of Fe–S bond, rendering difficult S incorporation to Fe–Si liquid structure (Morard et al. 2008). Even in the Fe–Ni–S–Si liquid in the miscible region, the strong interaction between Fe and S is also likely to exist and the interaction between S and Si to be weak. The K_{S0} of Fe–Ni–S–Si liquids decrease with increasing the relative concentration of light elements, X_S – X_{Si} (Fig. 6). If the Fe–Ni–S–Si liquid is a mixture of Fe–Ni–S and Fe–Ni–Si liquids, this trend can be interpreted by the idea that the elastic moduli of an aggregate of isotropic materials can be expressed as an integral of the modulus of elasticity of each component through volume (e.g., Hill 1952).

Implication to mercury core

Fe–Ni–S–Si alloy is the most plausible candidate that consists of the Mercury core (Malavergne et al. 2010; Smith et al. 2012; Hauck et al. 2013; Chabot et al. 2014). The size and chemical composition of the Mercury core can be constrained by searching the EOS of core material that matches the observed planet mass and moment of inertia (MOI). In previous studies, the size and composition of the Mercury core were estimated based on the EOS of binary Fe–alloys with using observed gravity field and spin state data. Estimated core radius and composition are 2004 ± 39 km for Fe–S core with 4.5 ± 1.8 wt% S (7.6 ± 2.9 at% S) (Rivoldini and Van Hoolst, 2013), and 1965–2050 km for Fe–S core with $4.6 + 2.5/- 2.0$ wt% S ($7.7 + 4.0/- 3.3$ at% S) or Fe–Si core with $10.5 + 3.3/- 3.7$ wt% Si ($18.9 + 5.2/- 6.2$ at% Si) (Terasaki et al. 2019). Hauck et al. (2013) estimated the size of Mercury Fe–S–Si core to be 2017 ± 29 km with outer core density ranging 3377 ± 201 kg/m³ from Monte Carlo internal structure model.

In this study, we determined the EOSs of Fe–Ni–S–Si ($\text{Fe}_{73}\text{Ni}_{10}\text{S}_{10}\text{Si}_7$ and $\text{Fe}_{72}\text{Ni}_{10}\text{S}_5\text{Si}_{13}$) liquids, which are in the suggested composition range of the Mercury core (Chabot et al. 2014). Based on these results, the effect of multiple light elements (S and Si) on the V_p and K_{S0} tends to be cancelled out each other in the range of S and Si contents of this study. This suggests that the V_p and K_{S0} are similar to those of liquid Fe and Fe–Ni. Therefore, if both S and Si are dissolved into the core, it could be difficult to identify the light element from V_p and elastic properties. On the other hand, if the amounts of S and Si are considerably different each other, i.e., the amount of S or Si is much more than the other light element, the difference in the V_p and elastic properties between S-rich liquid and Si-rich liquid could be identified. According to the possible compositional range of the Mercury core (Chabot et al. 2014), i.e., shaded area in Fig. 1, the Mercury core composition also covers the region where a large difference between

S and Si amounts, such as S-rich side ($S > 20$ wt% [29 at%], $\text{Si} < 5$ wt% [8 at%]), or Si-rich side ($S < 2$ wt% [3 at%], $\text{Si} > 10$ wt% [18 at%]). If the Mercury core is in these compositional ranges, we can probably distinguish whether S-rich or Si-rich core from V_p and elastic properties. The EOS of Fe–Ni–S–Si liquids with these compositions are required to be determined in future. In addition, other pairs of multiple light elements, such as S–C, Si–C, S–H, and Si–H, are still unclear for influence on the V_p and elastic properties.

If we can obtain the EOS of Fe–Ni–light elements liquids in arbitrary compositions, it is possible to strictly constrain the size and composition of the Mercury core by combining the measured data of Mercury mass and MOI. In late 2025, two BepiColombo space craft will arrive at Mercury. In this mission, more detailed and precise data of Mercury mass and MOI are also expected to be measured. To constrain the core size and composition by using these latest dataset, we need to establish the compositional dependence of the EOS of liquid Fe–Ni with multiple light elements in near future.

Conclusion

We measure the V_p of Fe–Ni–S–Si ($\text{Fe}_{73}\text{Ni}_{10}\text{S}_{10}\text{Si}_7$, $\text{Fe}_{72}\text{Ni}_{10}\text{S}_5\text{Si}_{13}$, $\text{Fe}_{67}\text{Ni}_{10}\text{S}_{10}\text{Si}_{13}$) liquids up to 17 GPa and 2000 K using the ultrasonic pulse-echo overlapping method with the multianvil press. The effect of temperature on the V_p is quite small in Fe–Ni–S–Si liquids. This trend is similar to Fe–S liquid. The effect of pressure on the V_p of Fe–Ni–S–Si liquids are smaller than those of Fe–Ni–S and Fe–Ni–Si liquids and close to that of liquid Fe. Obtained elastic properties using 3rd-order Birch–Murnaghan EOS are $K_{S0} = 99.1(9.4)$ GPa, $K_S' = 3.8(0.1)$ and $\rho_0 = 6.48$ g/cm³ for S-rich $\text{Fe}_{73}\text{Ni}_{10}\text{S}_{10}\text{Si}_7$ liquid and $K_{S0} = 112.1(1.5)$ GPa, $K_S' = 4.0(0.1)$ and $\rho_0 = 6.64$ g/cm³ for Si-rich $\text{Fe}_{72}\text{Ni}_{10}\text{S}_5\text{Si}_{13}$ liquid. In the present pressure range, the V_p of Fe–Ni–S–Si liquids of this study locate in between those of $\text{Fe}_{60}\text{Ni}_{10}\text{S}_{30}$ and $\text{Fe}_{52}\text{Ni}_{10}\text{Si}_{38}$ liquids and the V_p of Si-rich liquid is larger than that of S-rich liquid.

Comparing with the binary Fe–FeS ideal mixing model, the V_p of Fe–Ni–S–Si liquid deviate from that of Fe–FeS binary liquid at 1 atm and difference becomes to be small at 20 GPa. The K_{S0} of Fe–Ni–S–Si liquids decrease with increasing relative concentration of S and Si. This tendency is likely to reflect the mechanical mixing of Fe–S and Fe–Si liquids deriving from strong covalency of Fe–S bond.

If S and Si are dissolved simultaneously into the Mercury core in the compositional range of this study, the effect of S and Si on the elastic properties can be cancelled out each other, suggesting that it could be difficult to identify the light element in the core from V_p and elastic properties. However, if the amounts of S and Si are considerably different each other, we can probably distinguish whether S-rich or Si-rich

core. Thus, we need to determine the EOS of Fe–Ni–S–Si liquids in the compositions of S-rich side ($S > 20$ wt%, $Si < 5$ wt%), and Si-rich side ($S < 2$ wt%, $Si > 10$ wt%) to obtain the EOS in the Fe–Ni–S–Si system which covers entire range of possible Mercury core composition. This can be useful dataset to estimate the core composition combined with the geodesy data of upcoming Mercury mission.

Acknowledgements The authors acknowledge to K. Nishida, R. Saito, A. Kamiya, R. Tsuruoka, T. Sakaiya, Y. Katayama, and S. Kamada for their technical supports and discussions. The authors also thank to two anonymous reviewers for their constructive comments and suggestions. This work is partly supported by Grants-in-Aid for scientific research from the Ministry of Education, Culture, Sport, and Science and Technology (MEXT) of the Japanese Government to H. T. (no. 26247089, 20H02008). The synchrotron radiation experiments have been performed under contract of the SPring-8 facility (Proposal numbers: 2017A1317, 2017B1270, 2018A3781, 2018B1557, 2019A1740 and 2019B1403). This work was also partially supported by QST Advanced Characterization Nanotechnology Platform under the remit of "Nanotechnology Platform" of the MEXT, Japan (Proposal number: JPMXP09A18QS0013).

Author contributions I.Y. and H.T. performed measurements. H.T., I.Y., and S.U. wrote the main manuscript. I.Y., H.T., S.U., and T.K. discussed framework of this study. A.M., Y.T., and Y.H. supported experimental setups and measurements. All authors reviewed the manuscript.

Funding Open access funding provided by Okayama University.

Data availability The data for this paper are listed in Tables 1 and 2 and also available by contacting the corresponding author H. T. at tera@okayama-u.ac.jp

Declarations

Competing interests The authors declare no competing interests.

Open Access This article is licensed under a Creative Commons Attribution 4.0 International License, which permits use, sharing, adaptation, distribution and reproduction in any medium or format, as long as you give appropriate credit to the original author(s) and the source, provide a link to the Creative Commons licence, and indicate if changes were made. The images or other third party material in this article are included in the article's Creative Commons licence, unless indicated otherwise in a credit line to the material. If material is not included in the article's Creative Commons licence and your intended use is not permitted by statutory regulation or exceeds the permitted use, you will need to obtain permission directly from the copyright holder. To view a copy of this licence, visit <http://creativecommons.org/licenses/by/4.0/>.

References

- Anderson WW, Ahrens TJ (1994) An equation of state for liquid iron and implications for the Earth's core. *J Geophys Res* 99:4273–4284
- Antonangeli D, Morard G, Schmerr NC, Komabayashi T, Krisch M, Fiquet G, Fei Y (2015) Toward a mineral physics reference model for the Moon's core. *Proc Nat Acad Sci* 112(13):3916–3919
- Chabot NL, Wollack EA, Kima RL, Minitti ME (2014) Experimental constraints on Mercury's core composition. *Earth Planet Sci Lett* 390:199–208
- Dumay C, Cramb AW (1995) Density and interfacial tension of liquid Fe–Si alloys. *Metall Mat Trans B* 26B:173–176
- Hauck SA, Margot JL, Solomon SC, Phillips RJ, Johnson CL, Lemoine FG, Mazarico E, McCoy TJ, Padovan S, Peale SJ, Perry ME, Smith DE, Zuber MT (2013) The curious case of Mercury's internal structure. *J Geophys Res: Planets* 118:1204–1220
- Higo Y, Kono Y, Inoue T, Irifune T, Funakoshi K (2009) A system for measuring elastic wave velocity under high pressure and high temperature using a combination of ultrasonic measurement and the multi-anvil apparatus at SPring-8. *J Synchr Rad* 16(6):762–768
- Hill R (1952) The elastic behavior of a crystalline aggregate. *Proc Phys Soc A65*:349–354
- Hirose K, Labrosse S, Hernlund J (2013) Composition and state of the core. *Ann Rev Earth Planet Sci* 41:657–691
- Jing Z, Wang Y, Kono Y, Yu T, Sakamaki T, Park C, Rivers ML, Sutton SR, Shen G (2014) Sound velocity of Fe–S liquids at high pressure: Implications for the Moon's molten outer core. *Earth Planet Sci Lett* 396:78–87
- Kaiura GH, Toguri JM (1979) Densities of the molten FeS, FeS–Cu₂S and Fe–S–O systems—Utilizing a bottom-balance Archimedean technique. *Can Metall Quart* 18(2):155–164
- Kawaguchi SI, Nakajima Y, Hirose K, Komabayashi T, Ozawa H, Tateno S, Kuwayama Y, Tsutsui S, Baron AQR (2017) Sound velocity of liquid Fe–Ni–S at high pressure. *J Geophys Res: Solid Earth* 122:3624–3634
- Kawai Y, Mori K, Kishimoto M, Ishikura K, Shimoda S (1974) Surface tension of liquid Fe–C–Si alloys (In Japanese text with English abstract). *Tetsu to Hagane* 60(1):29–37
- Kono Y, Park C, Sakamaki T, Kenny-Benson C, Shen G, Wang Y (2012) Simultaneous structure and elastic wave velocity measurement of SiO₂ glass at high pressures and high temperatures in a Paris-Edinburgh cell. *Rev Sci Instr* 83:033905
- Kuwabara S, Terasaki H, Nihida K, Shimoyama Y, Takubo Y, Higo Y, Shibasaki Y, Urakawa S, Uesugi K, Takeuchi A, Kondo T (2016) Sound velocity and elastic properties of Fe–Ni and Fe–Ni–C liquidus at high pressure. *Phys Chem Mineral* 43:229–236
- Malavergne V, Toplis MJ, Berthet S, Jones J (2010) Highly reducing conditions during core formation on Mercury: Implications for internal structure and the origin of a magnetic field. *Icarus* 206:199–209
- Margot JL, Peale SJ, Jurgens RF, Slade MA, Holin IV (2007) large longitude libration of Mercury reveals a molten core. *Science* 319:710–714
- Matsui M (2009) Temperature–pressure–volume equation of state of the B1 phase of sodium chloride. *Phys Earth Planet Inter* 174(1–4):93–97
- Morard G, Katsura T (2010) Pressure–temperature cartography of Fe–S–Si immiscible system. *Geochim Cosmochim Acta* 74:3659–3667
- Morard G, Sanloup C, Guillot B, Fiquet G, Mezouar M, Perrillat JP, Garbarino G, Mibe K, Komabayashi T, Funakoshi K (2008) In situ structural investigation of Fe–Si–S immiscible liquid system and evolution of Fe–S bond properties with pressure. *J Geophys Res* 113:B10205. <https://doi.org/10.1029/2008JB005663>
- Morard G, Bouchet J, Rivoldini A, Antonangeli D, Reberge M, Boulard E, Denoué A, Mezouar M (2018) Liquid properties in the Fe–FeS system under moderate pressure: Tool box to model small planetary cores. *Ame Mineral* 103:1770–1779
- Nagamori M (1969) Density of molten Ag–S, Cu–S, Fe–S, and Ni–S systems. *Trans Metall Soc AIME* 245:1897–1902
- Nakajima Y, Imada S, Hirose K, Komabayashi T, Ozawa H, Tateno S, Tsutsui S, Kuwayama Y, Baron AQR (2015) Carbon-depleted outer core revealed by sound velocity measurements of liquid iron–carbon alloy. *Nat Comm* 6:8942
- Nasch PM, Manghnani MH, Secco RA (1997) Anomalous behavior of sound velocity and attenuation in liquid Fe–Ni–S. *Science* 277:219–221

- Nishida K, Kono Y, Terasaki H, Takahashi S, Ishii M, Shimoyama Y, Higo Y, Funakoshi K, Irifune T, Ohtani E (2013) Sound velocity measurement in liquid Fe-S at high pressure: Implications for Earth's and lunar cores. *Earth Planet Sci Lett* 362:182–186
- Nishida K, Suzuki A, Terasaki H, Shibazaki Y, Higo Y, Kuwabara S, Shimoyama Y, Sakurai M, Ushioda M, Takahashi E, Kikegawa T, Wakabayashi D, Funamori N (2016) Towards a consensus on the pressure and composition dependence of sound velocity in the liquid Fe-S system. *Phys Earth Planet Inter* 257:230–239
- Nishida K, Shibazaki Y, Terasaki H, Higo Y, Suzuki A, Funamori N, Hirose K (2020) Effect of sulfur on sound velocity of liquid iron under Martian core conditions. *Nat Comm* 11:1954
- Nittler LR, Starrm RD, Weider SZ, McCoy TJ, Boynton WV, Ebel DS, Ernst CM, Evans LG, Goldsten JO, Hamara DK, Lawrence DJ, McNutt RL Jr, Schlemm CE II, Solomon SC, Sprague AL (2011) The major-element composition of Mercury's surface from MESSENGER X-ray spectrometry. *Science* 333:1847–1850
- Rivoldini A, Van Hoolst T, Verhoeven O, Mocquet A, Dehant V (2011) Geodesy constraints on the interior structure and composition of Mars. *Icarus* 213: 451–472
- Rivoldini A, Van Hoolst T (2013) The interior structure of Mercury constrained by the low-degree gravity field and the rotation of Mercury. *Earth Planet Sci Lett* 377–378:62–72
- Sata N, Shen G, Rivers ML, Sutton SR (2002) Pressure-volume equation of state of the high-pressure B2 phase of NaCl. *Phys Rev B* 65:104114
- Shibazaki Y, Kono Y (2018) Effect of silicon, carbon, sulfur on structure of liquid iron and implications for structure-property relations in liquid iron-light element alloys. *J Geophys Res: Solid Earth* 123:4697–4706
- Shimoyama Y, Terasaki H, Urakawa S, Takubo Y, Kuwabara S, Kishimoto S, Watanuki T, Machida A, Katayama Y, Kondo T (2016) Thermoelastic properties of liquid Fe-C revealed by sound velocity and density measurements at high pressure. *J Geophys Res: Solid Earth* 121:7984–7995
- Shobu T, Tozawa K, Shiwaku H, Konishi H, Inami T, Harami T, Mizuki J (2007) Wide band energy beamline using Si(111) crystal monochrometers at BL22XU in SPring-8. *AIP Conf Proc* 879:902
- Smith DE, Zuber MT, Phillips RJ, Solomon SC, Hauck SA II, Lemoine FG, Mazarico E, Johnson CL, Torrence MH, Perry ME, Rowlands DD, Goossens S, Head JW, Taylor AH (2012) Gravity field and internal structure of Mercury from MESSENGER. *Science* 336:214–217
- Tange Y, Nishihara Y, Tsuchiya T (2009) Unified analyses for P-V-T equation of state of MgO: A solution for pressure-scale problems in high P-T experiments. *J Geophys Res: Solid Earth* 114:B03208
- Terasaki H, Rivoldini A, Shimoyama Y, Nishida K, Urakawa S, Maki M, Kurokawa F, Takubo Y, Shibazaki Y, Sakamaki T, Machida A, Higo Y, Uesugi K, Takeuchi A, Watanuki T, Kondo T (2019) Pressure and composition effects on sound velocity and density of core-forming liquids: Implication to core compositions of terrestrial planets. *J Geophys Res: Planets* 124:2272–2293
- Terasaki H, Nishida K (2018) Density and elasticity measurements for liquid materials. In: Kono Y, Sanloup C (eds) *Magma under pressure*, 237–260
- Wakabayashi D, Funamori N (2015) Solving the problem of inconsistency in the reported equations of state for h-BN. *High Press Res* 35(2):123–129
- Williams Q, Manghnani MH, Secco RA, Fu S (2015) Limitations on silicon in the outer core: Ultrasonic measurements at high temperatures and high dK/dP values of Fe-Ni-Si liquids at high pressures. *J Geophys Res: Solid Earth* 120:6846–6855
- Yoshizaki T, McDonough WF (2020) The composition of Mars. *Geochim Cosmochim Acta* 273:137–162
- Yu X, Secco RA (2008) Equation of state of liquid Fe–17 wt%Si to 12GPa. *High Press Res* 28(1):19–28

Publisher's Note Springer Nature remains neutral with regard to jurisdictional claims in published maps and institutional affiliations.